Cold Regions Science and Technology 76–77 (2012) 17–23

Contents lists available at ScienceDirect

Cold Regions Science and Technology

journal homepage: www.elsevier.com/locate/coldregions

Deformation of the Arctic Ocean ice cover after the 2007 record minimum in summer ice extent

R. Kwok *, G.F. Cunningham

Jet Propulsion Laboratory, California Institute of Technology, Pasadena, CA, USA

ARTICLE INFO

Article history:
Received 10 February 2011
Accepted 11 April 2011

Keywords:
Arctic Ocean sea ice
Sea ice deformation
Mass balance

ABSTRACT

We examine the deformation of the Arctic Ocean sea ice cover after the record minimum in summer extent in 2007. The period spans ~2.5 months between September 15 and December 1. Ice drift and deformation inside the ice edge, within a domain that initially covers $\sim 0.76 \times 10^6$ km^2 of the western Arctic, are derived from high-resolution RADARSAT imagery from the Alaska Satellite Facility. Poleward of 80°N, we find a net convergence of more than 14% over the period. This large convergence is associated with the strength, location, and persistence of the Beaufort high-pressure pattern that led to prevailing on-shore winds north of Ellesmere Island and Greenland. This can be contrasted to the nearly 25% divergence of the ice cover, accompanied by a large regional vorticity of −0.93 (or a clockwise rotation of ~53°) south of 80°N. The same atmospheric pattern produced openings as the ice cover drifts southwest towards the unconstrained ice-free part of the southern Beaufort and Chukchi Seas. These sustained strain rates, especially convergence, impacts the area and thickness distribution of the sea ice cover in the Arctic Basin. If unaccounted for, this deformation-induced decrease in ice coverage (in this region with predominantly multiyear ice) could be incorrectly ascribed to ice export with a concurrent decrease in Arctic sea ice volume, when in fact the ice volume is conserved but with a local redistribution in thickness.

1. Introduction

The seasonal cycle of sea ice deformation in the Arctic Ocean, from 12-years of high-resolution ice kinematics produced by the RADARSAT Geophysical Processor System (RGPS), is shown in Fig. 1. A distinct seasonal cycle is clearly seen in both the seasonal and multiyear ice zones; the peak in deformation observed in the late fall is followed by seasonal minimums in the late winter when the ice cover is thickest and constrained by land boundaries. In addition to the seasonal cycle, Kwok (2006) contrasted the higher deformation, with its increased deformation-induced ice production, observed in the first-year zone compared with that in the older, thicker, multiyear ice zone during the late fall and winter. Sometime after melt onset, the results in the figure also suggest that the mean deformation characteristics of the two ice zones converge; there is less distinction between these zones as the ice cover becomes less compact and weaker because of negligible ice growth in openings during the summer.

What is of interest is how the ice cover behaves after significant thinning at the end the summer (i.e., late September through early December). The first-year and multiyear sea ice that survives the summer is at its thinnest and mechanically weakest at the beginning of the growth season. As the amount of deformation is dependent on ice strength, the response of the ice cover to external forcing should be particularly pronounced in the fall. The summer of 2007 offers an opportunity to explore this response. In September 2007, the summer ice extent reached a record minimum of 4.2×10^6 km^2, which was 1.6×10^6 km^2 or 23% less than the previous record set in September 2005 (Stroeve et al., 2007). The summer retreat was largest in the East Siberian, Chukchi, and Beaufort Seas. Nearly 40% of the Arctic basin was covered by open-ocean at the end of the 2007 summer. In parallel, there was an overall thinning of ~0.5 m between those two record-setting years (Kwok et al., 2009). Hence, these ice condition in 2007 provide a glimpse at the potentially extreme dynamic response of the ice cover as it thins.

Why is this of interest? If the significant deformation at the beginning of the growth season were unaccounted for in the mass and area balance of ice cover, any deformation-induced decrease in ice coverage could be incorrectly attributed to ice export with a concurrent decrease in Arctic sea ice volume when in fact the ice volume is conserved but compensated by redistributions in thickness. It should be recognized that the MYI at the end of summer maybe thinner and more prone to deformation. Thus, this may affect the interpretation of MYI coverage within the Arctic basin. Additionally, the rate of deformation-induced ice production and the changes in ice thickness distributions affect the survivability of the ice cover in the subsequent melt seasons. This is of particular interest if the ice cover continues to thin in the coming decade.

The aim of this paper is to quantify the deformation of the ice cover after the summer of 2007. The sampling of this time of the year in the

* Corresponding author. Tel.: +1 8183545614; fax: +1 8183933077.
E-mail address: ron.kwok@jpl.nasa.gov (R. Kwok).

0165-232X/$ – see front matter © 2011 Elsevier B.V. All rights reserved.
doi:10.1016/j.coldregions.2011.04.003

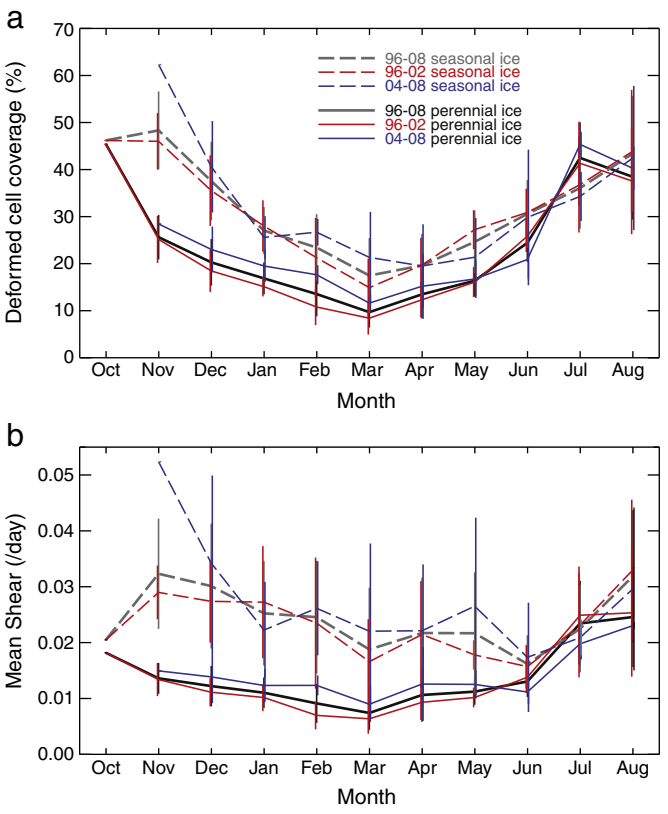

Fig. 1. Seasonal cycle of deformation over first-year and multiyear Arctic sea ice from RGPS kinematics (1996–2008). (a) Percentage of deformed cell coverage. (b) Mean shear. A cell is considered active (deformed) over a time step if the magnitude of divergence is greater than 0.02/day or the magnitude of shear is greater than 0.03/day. The line plots show the mean and standard deviation over the entire dataset (1996–2008), between 1996 and 2002, and between 2004 and 2008.

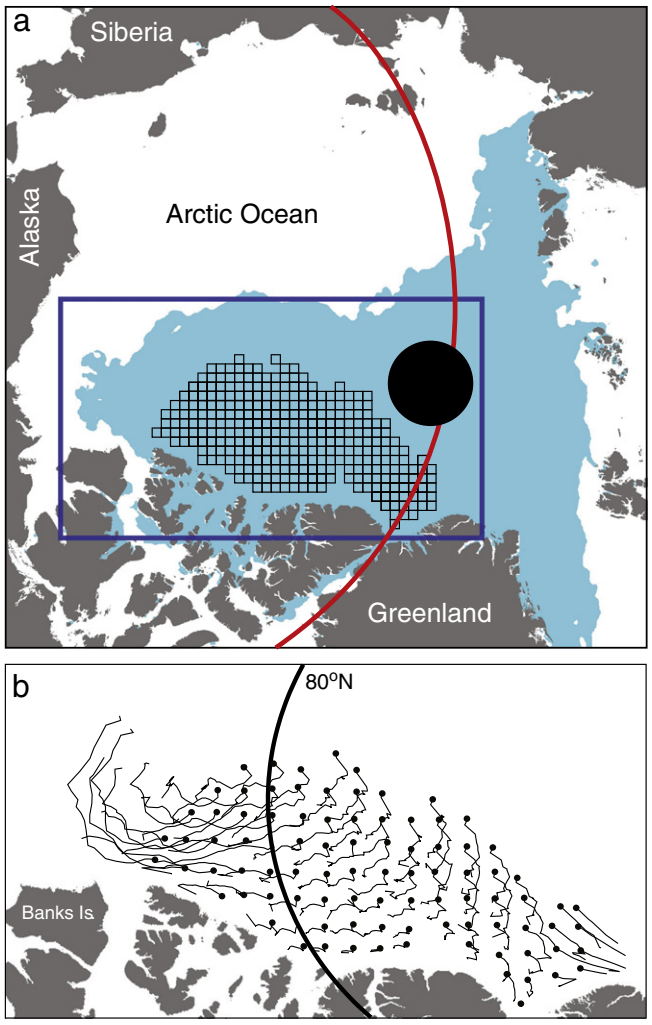

Fig. 2. Sampling of ice drift from the end of summer (start date: September 15, 2007) through the beginning of December. (a) The initial region (50-km grid) is shown in black. The drift of sea ice originally at the grid vertices is tracked for a period of 2.5 months. The light blue region is the ice extent near summer minimum (September 15). The red circle shows the approximate limit of reception mask of the Alaska Satellite Facility. Image data are not available within the black circle due to orbit inclination. These two factors constrain the broader sampling of the motion field. (b) The trajectories of ice drift, over the period, from the RGPS motion tracker within a box that is 2300 km by 1300 km. Black dot indicates the beginning of a trajectory. Only every other one is shown.

available RGPS data set is particularly poor due to tracking issues associated with variable ice signatures and deformation at the end of summer. As part of this work, we develop an ice kinematics data set that is more suited for our present investigation. This paper is organized as follows. The data sets used in this analysis are listed in the next section. Section 3 describes our strategy for selecting the region of interest and our approach in sampling the ice drift in the high-resolution radar imagery. Section 4 summarizes our analysis of the deformation computed from the time series of measured ice drift. The last section discusses the implications of results and how this bears on the interpretation of remote sensing data sets of the Arctic Ocean ice cover.

2. Data description

The time-series of high-resolution SAR imagery and other datasets used in supporting our analysis are described here.

2.1. RADARSAT-1 imagery

Ice drift is derived from RADARSAT-1 SAR imagery (spatial resolution: ~150 m) by computing the displacement of common ice features in time-separated backscatter fields using an image matching procedure described by Kwok et al. (1990). The selection of a region of interest (or domain) and the strategy for deriving ice drift are described in the next section. The C-band RADARSAT-1 image sequence used here is recorded, processed, calibrated, and distributed by the Alaska Satellite Facility (ASF). The coverage of the Arctic Ocean within the reception ASF mask (see Fig. 2a), over the 2.5-month period, is nominally 3 days although a small number of the acquisitions – due to operational constraints – are over a longer interval (i.e., 4 to 6 days). Data from the wide-swath imaging capability of the radar (~450 km ScanSAR-wide mode) are used to maximize coverage of the region of interest.

2.2. Other datasets

The secondary data sets include: 1) Analyzed fields of multiyear ice (MYI) concentration from QuikSCAT; 2) Daily fields of sea ice motion and ice concentration from the Advanced Microwave Scanning Radiometer (AMSR-E); and 3) Sea level pressure (SLP) fields from NCEP/NCAR. Estimation and assessment of the spatial distribution of MYI coverage from the scatterometer fields are described in Kwok (2004). Since this type of analysis is more reliable after the backscatter signatures stabilize later in November when the ice and snow covers become cold (<10 °C), the MYI fields are used only during the latter part of the period. The analyzed MYI fields are useful for illustrating the impact of regional convergence on area/coverage estimates.

Satellite passive microwave ice concentrations from the AMSR Bootstrap-algorithm are used here. Passive microwave ice motion fields are those described by Kwok et al. (1998) and Kwok (2008). These large-scale motion fields and the analyzed meteorological fields provide a basin-scale view of the wind forcing and circulation patterns of the Arctic Ocean, and a spatial context for understanding the small-scale ice drift from the SAR imagery.

3. Approach

3.1. Region of interest and ice tracking strategy

The objective is to sample those parts of the ice cover where SAR imagery is available (i.e., within the ASF reception mask) and where the ice tracking system can produce reliable estimates of ice drift. At the end of summer, when the ice concentrations are low and the backscatter signatures are variable, especially near the ice edge, the uncertainties in the tracking results are higher. With consideration of these factors, we positioned an initial grid on the ice cover that is approximately 200 km inside the ice edge on September 15 — roughly the day of minimum ice extent (see Fig. 2a). The average ice concentration within the grid is over 98% on that date — this ensures a relatively compact ice cover with lower deformation between time steps thus improving the quality of the ice drift estimates. By definition, most of this ice is referred to as multiyear ice regardless of its thickness. The region extends ~700 km into the Arctic Ocean from the coasts of Greenland, Ellesmere Island, and the Canadian Arctic Archipelago. For monitoring the quality of the derived motion vectors, the tracking system produces a set of quality metrics including those derived from image matching and on the expected deformation of the local grid (Kwok & Cunningham, 2000). All motion vectors are visually inspected with special attention paid to the low quality estimates. Erroneous motion vectors are corrected or replaced where needed.

To produce a record of the geometry of the ice parcels for constructing a time series of ice deformation, we trace the displacements of an array of ice particles starting at their initial locations on a uniform grid (50 km on a side). The period examined spans ~2.5 months between September 15 and December 1. Grid spacing is selected to reduce the computational load and the burden of visual inspection for controlling data quality. The entire grid (Fig. 2a) contains 304 ice parcels or cells (as defined by the grid vertices) that covers an area of $\sim 0.76 \times 10^6\,\mathrm{km}^2$ of the Arctic. The spatial density of the grid can be seen in Fig. 2a. Based on expected revisits of the radar platform, the trajectory of individual ice parcels are typically sampled every three days. This interval, however, could vary by several days as discussed earlier.

3.2. Trajectories and deformation

Fig. 2b shows the drift trajectories of sea ice starting from their initial locations on the 50-km grid and their final locations on December 1. Uncertainties in the tracking are between 100–300 m (Kwok & Cunningham, 2002; Lindsay & Stern, 2003), comparable to those obtained with buoy data.

The divergence, vorticity, and shear of each cell for each time step are computed via:

$$\nabla \cdot u = u_x + v_y, \quad \zeta = v_x - u_y, \quad e = \left[\left(u_x - v_y \right)^2 + \left(u_y + v_x \right)^2 \right]^{\frac{1}{2}}$$

u_x, u_y, v_x, v_y are the spatial gradients in ice motion computed using a line integral around the boundary of each cell (~50 km on a side

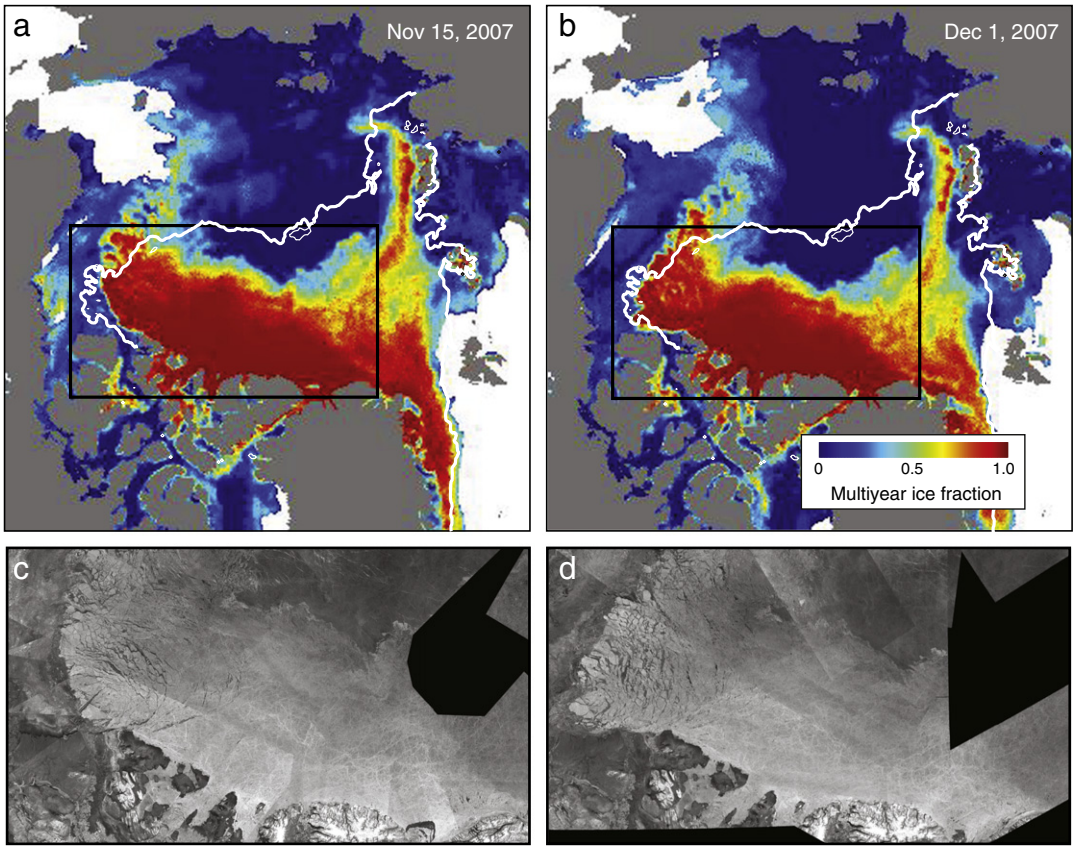

Fig. 3. The Arctic sea ice cover from QuikSCAT and RADARSAT. (a) Analyzed multiyear ice fraction on Nov 15, 2007 (from QuikSCAT). (b) Multiyear ice fraction on December 1, 2007. (c) RADARSAT mosaic of the Arctic Ocean within the rectangle in (a) on Nov 15. (d) Same as (c) but on Dec 1. White outline shows the ice edge during summer minimum. (RADARSAT imagery ©CSA 2011).

initially) (Kwok, 2006). The line segments connecting the four vertices of a cell define the boundaries.$\nabla \cdot u$ is a measure of cell area change, ζ is the principle measure of rotation, and e is the scalar magnitude of shear.

We note that the sides of these cells are not the actual boundaries of the material element. Floes smaller than the cell dimensions could advect into and out of these boundaries. Inspection of SAR imagery shows that this does not happen often since most deformations, within the pack, occur along leads between rigid plates and independent motion of small floes are not typical after freeze-up. An associated spatial sampling issue is that the area change of a cell is interpreted as caused by a single type of event — opening or closing. If there were a mix of opening and closing events within a 50 km by 50 km cell producing the same net area change, these events would not be sampled correctly. But, for the purposes here, we are more interested in measuring the net change over the region rather than the details of individual opening and closing events. For the area of a 50 km × 50 km ice parcel, an expected uncertainty of 100 m in the daily displacement introduces a very small error (or noise) in divergence, i.e., 6×10^{-3}/day or $6.5\times10^{-8}s^{-1}$. The average uncertainty for 300 cells, scaled by $1/\sqrt{N}$ reduces to 3.4×10^{-4}/day. This can be compared to the magnitude of regional strain rates ($\sim5\times10^{-3}$/day), discussed herein, that is observed over the period of interest discussed here.

4. Results

4.1. Ice conditions — multiyear sea ice coverage

Fig. 3 shows the analysis of multiyear ice coverage from QuikSCAT and the September 15 ice edge (white outline) from AMSR-E. The high-resolution RADARSAT mosaics (Fig. 3c and d) serve to highlight the more detailed ice conditions and as a measure of the reliability of the MYI analysis from QuikSCAT. The high intensity pixels in the RADARAT imagery are signatures of MYI while the lower intensity pixels are indicative of first-year ice (FYI). The spatial correspondence in the location of the V-shaped backscatter-delineated MYI margins in the RADARSAT mosaics and the edge of the multiyear pack in the lower resolution QuikSCAT analysis is clear.

As anticipated, the shape of the AMSR-E ice edge at the end of summer resembles the edge of the MYI cover except for the displacement of that edge towards the coast of Greenland and Ellesmere Island. Also apparent is the reduced concentration of MYI west of Banks Island between September and November. These on-shore displacements suggest a fairly large convergence of the MYI zone north of Greenland as well as divergence and westward advection of the MYI zone further south. Even during the two weeks between November 15 and December 1, significant deformation and rotation of the MYI pack are quite evident (in Fig. 3c and d). In the following analysis, we quantify the role of deformation in these changes using the ice kinematics developed using RADARSAT imagery.

4.2. Trajectories and large scale circulation

The diversity in the ice motion over the 2.5 months is captured in the field of drift trajectories in Fig. 2. Gradients in the near-coast ice motion, with slower movements near-shore, are clearly seen. Just north of the Lincoln Sea, sometimes referred to as the switchyard of the Arctic Ocean, the ice splits and moves in three distinct directions as the ice cover converges and separates north of the coast of Greenland and Ellesmere Island. A fraction of the ice cover exits the eastern boundary of our domain and moves towards the Fram Strait. Another fraction continues

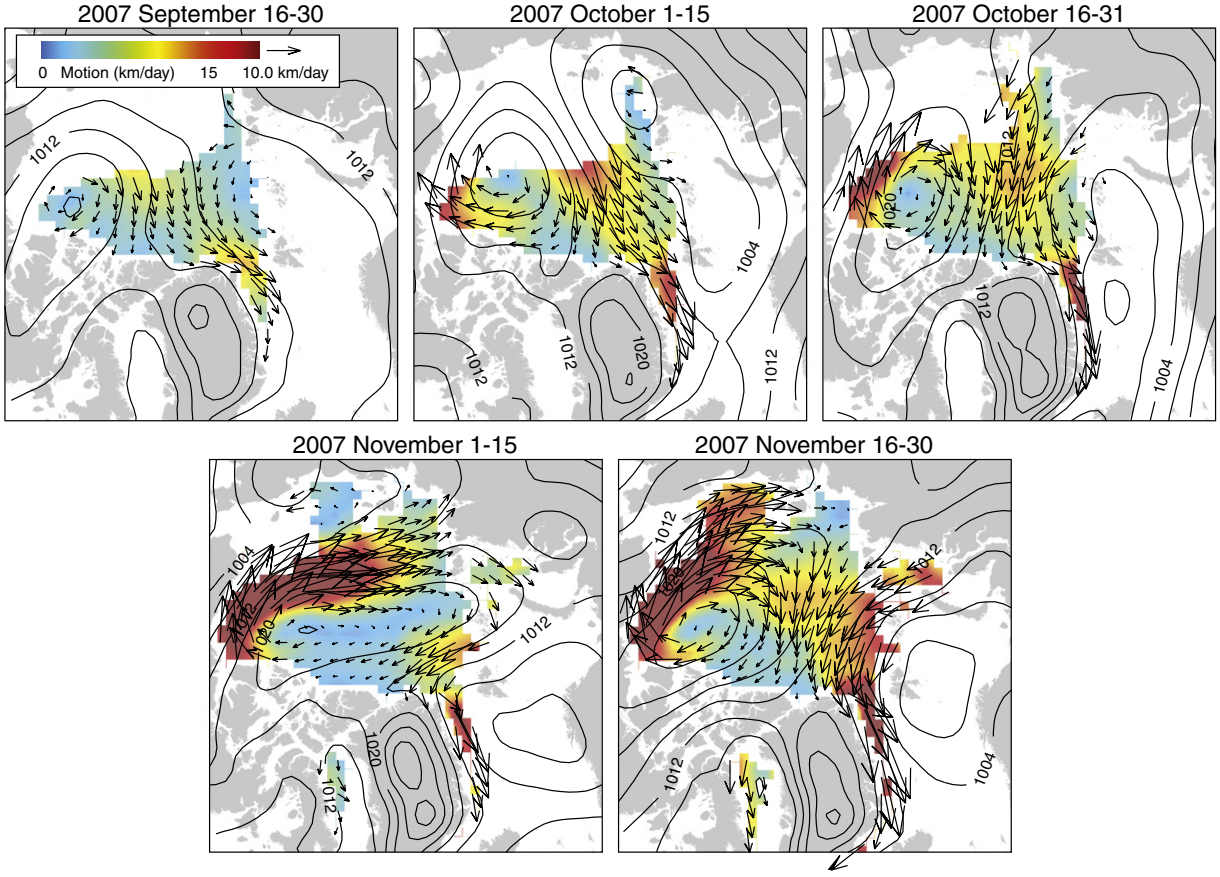

Fig. 4. (a) Mean (2-week) motion fields of the Arctic Ocean over the 2.5-month period. Isobars on the motion fields are of sea level pressure (contour interval: 4 hPa).

south into the Lincoln Sea where some fraction of that enters the Nares Strait. During this period in 2007, there were no ice arches along Nares Strait to block southward ice motion and the export of thick MYI ice into Baffin Bay (Kwok et al., 2010). The dominant fraction drifts south before turning off-shore and westward just north of Banks Island. The magnitude of this westward drift and the motion gradient within 100 km of the coast of Ellesmere Island and the Canadian Arctic Archipelago are especially remarkable (Fig. 4).

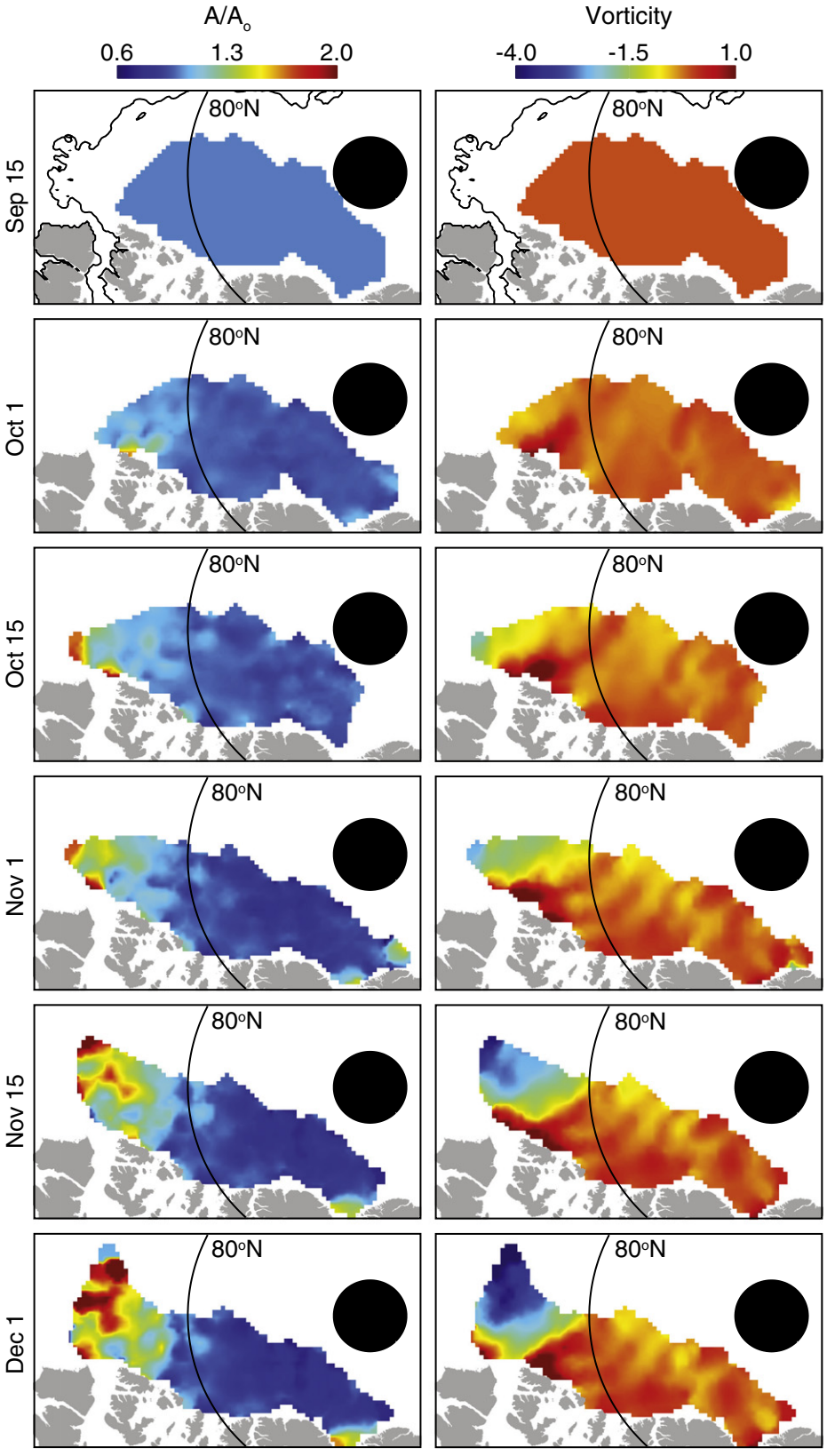

Fig. 5. Spatial distribution of cumulative divergence and vorticity from September 15 through December 1 as sampled by the Lagrangian cells.

The observed ice drift can be related to the large-scale wind-driven circulation of the ice cover. Fig. 3 shows the 2-weekly mean fields of sea level pressure distribution and gridded ice motion, as well as the mean ice extent, over the period. At the beginning of December, there are still large expanses of open water in the Chukchi Sea. In four of the five 2-weekly fields, we find a persistent and intense high-pressure pattern centered in the Beaufort Sea with a trough of low pressure in the eastern Arctic Ocean. Prevailing on-shore winds that push the ice cover against the coast of Greenland and Ellesmere Island are associated with this arrangement and distribution in SLP. The anti-cyclonic circulation pattern associated with the high also drives the ice southward and then westward toward the Beaufort and Chukchi Seas. Drift trajectories show large clockwise rotations of the ice cover. How the ice cover responds to this forcing is discussed next.

4.3. Patterns of cumulative divergence and vorticity

The spatial fields of cumulative divergence and vorticity as sampled by the material elements at the beginning and middle of each month are shown in Fig. 5. Cumulative divergence and vorticity of each cell, between two observations (at t_1 and t_2), are calculated by first summing the four velocity gradients over the period of interest. The mechanical expressions of the ice cover response to the atmospheric forcing pattern (discussed earlier) are evident by contrasting the deformation patterns in the initial (Sep-15) and final (Dec-1) fields.

Poleward of 80°N, the ice cover is convergent almost everywhere as a result of the on-shore winds and ice motion over the period. The coherent displacement of the edge of the region towards the Ellesmere/Greenland coast is apparent. Also of note is the quasi-regular banding in the vorticity field that is characteristic of the typical angular orientation of the lead/fracture patterns that form relative to rigid coastal boundaries (Fig. 5 — Nov 1); these have been observed AVHRR, passive microwave, and high-resolution radar imagery (Kwok, 2001).

At roughly 80°N, the fields show distinct transitions from a largely convergent zone to one of low divergence during the latter half of the period. The transition from a moderate vorticity region in the north to one with large negative vorticity (clockwise rotation) is even more pronounced, again a consequence of the circulation pattern relative to the coastal boundaries.

South of 80°N, the deformation character is markedly different. The fields are non-convergent. Near the end of the period, the westward advection and the large divergence of the ice parcels at the southern tip of our region is particularly noticeable; this can be seen in the drift trajectories in Fig. 2. Openings can be seen as increases in density and extent of fractures (dark linear features) in the SAR imagery between the two periods (see Fig. 3). The low backscatter pixels in the radar data are signatures of seasonal ice formed in the large fractures between MYI floes. The compactness or concentration of the MYI is reduced as a consequence.

The region of the domain that advected into the Lincoln Sea shows significant divergence as large ice floes are broken off of the thick MYI pack before exiting the Arctic Ocean through the Robson Channel and Nares Strait before exiting into Baffin Bay (Kwok et al., 2010).

4.4. Strain rates

The line plots in Fig. 6 show the time-series of deformation (divergence, vorticity, and shear) of the region at near 3-day intervals as well as the cumulative deformation over the 2.5-month period. The net regional divergence and vorticity of the material elements within the domain are ~3% and −0.43 (or a clockwise rotation of 25°). As expected, the mean shear cumulates over the period. Based on the contrast observed in the spatial field (in Fig. 5) discussed above, we examine the regional deformation poleward and south of 80°N to obtain more quantitative insights into the differences. The boundaries of the two regions do not enclose the same areas.

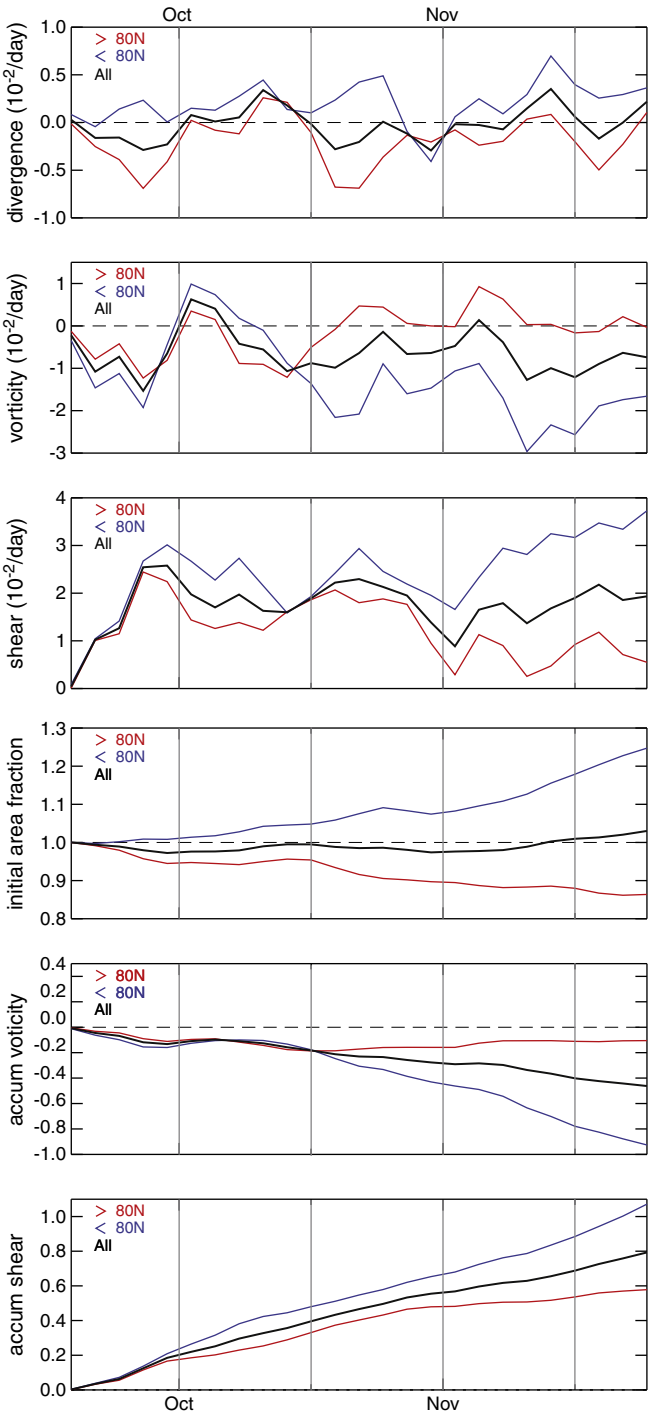

Fig. 6. Time series of regional deformation. (a) 3-day deformation of the Lagrangian cells defined by the grid vertices. (c) Cumulative deformation (area, vorticity, and shear) of the ice cover. The line plots summarize the overall (black), as well as those above (red) and below 80°N (blue), behavior of Lagrangian cells.

Poleward of 80°N, we find a net convergence of more than 14% over the period due to three identifiable episodes: two occurred during the latter halves of September and October, and one after mid-November. These can be seen in the large-scale circulation plots in Fig. 3, which show that the strength of the on-shore flow is especially strong. The net vorticity over the period is relatively small: −0.1 (~6°). Initially, the shear in this region is high but is lower at the end of period; this is likely due to the mechanical strengthening associated with ice growth and ridging.

This can be contrasted to the nearly 25% divergence of the ice cover, accompanied by a large cumulative vorticity of the ice cover of −0.93 (or a clockwise rotation of ~53°) south of 80°N. The time series shows a positive trend in divergence over the period with sustained negative vorticity due the Beaufort High. Also, the mean shear of the region builds as the compactness and strength of the MYI cover are reduced due to divergence.

5. Conclusions

In this paper, we examined the regional deformation of the Arctic Ocean sea ice cover, over a 2.5-month period, after the record minimum in summer extent in 2007. High-resolution ice drift from a sequence of radar imagery from RADARSAT provides a glimpse of how the ice cover behaved after the significant thinning at the end this record-setting summer. The region, covering an initial area of $\sim 0.76 \times 10^6 km^2$ of predominantly multiyear ice, extends ~700 km into the Arctic Ocean from the coasts of Greenland, Ellesmere Island, and the Canadian Arctic Archipelago.

The net divergence and vorticity of the region are ~3% and −0.43 (or a clockwise rotation of 25°), respectively. Overall, the ice cover within our domain is divergent with a rotation in the same sense as that of circulation pattern imparted by the persistent high SLP pattern centered in the southern Beaufort Sea. Even though the overall deformation seems moderate, there are two distinct regimes of ice motion and deformation with differing characteristics that contributed to the observed mean: one poleward of 80°N and the other to the south. Poleward of 80°N, we find a net convergence of more than 14% over the period that is a result of the strain rates associated with the response to on-shore wind and motion. This can be contrasted to the nearly 25% divergence of the ice cover, accompanied by a large regional vorticity of −0.93 (or a clockwise rotation of ~53°) south of 80°N. The significant southwest drift north of Banks Island is towards the unconstrained ice-free part of the southern Beaufort and Chukchi Seas. This resulted in a more fragmented ice cover with large fractures (visible in SAR imager) that separate large MYI ice floes.

From an observations perspective, the regional extent and fractional coverage of MYI are being routinely monitored with rather coarse spaceborne scatterometers. It should be recognized that the MYI at the end of recent summers are thinner and more prone to deformation. Thus, this may affect the interpretation of changes MYI coverage within the Arctic basin. The deformation-induced changes in MYI extent and coverage, if unaccounted for, could be incorrectly ascribed to ice export with a concurrent decrease in Arctic sea ice volume; only the ice thickness distribution is altered in the mechanical redistribution of sea ice. With a thinner and weaker MYI cover, care should be taken in the interpretation of the time-varying area of MYI coverage within the Arctic. Even though we started with a relatively compact ice cover (>98%) with largely MYI at the end of summer, it should be noted the relative fraction of MY vs. FY ice ridging is not resolved in our analysis.

The fragmentation of the MYI cover, south of 80°N, continued throughout the season and can be seen clearly in Fig. 1b in Kwok and Cunningham (2010). A large fraction of the broken up MYI pack that spread out over a large area of the Beaufort Sea at the onset of melt (on April 30, 2008) was lost to melt during the summer. In fact, the melt of MYI area of $213 \times 10^6 km^2$ in the Beaufort Sea was the highest over the 17-year period between 1993–2009. This highlights the consequence and importance of lateral melt during the summer – as the open water between the floes warms quickly – if the consolidated MYI cover was broken up during winter storms before or during the melt season.

The strain rates observed here have large impact on the area and thickness distribution of the sea ice cover in the Arctic Basin. From a mass balance perspective, this emphasizes the potentially large variability in regional ice thickness that could occur in a short period of time due to mechanical and advective redistribution of ice volume. Divergence adds to the thin end of the distribution while convergence adds to the other extreme.

While it is clear that deformation-related ice production contributes positively to the mass budget, its overall effect in the face of increasing seasonal and thinner/weaker sea ice coverage may be more complicated (Kwok, 2006). By decreasing the stability of the water column and thus promoting overturning with warmer, deeper waters, the brine rejection might also act to keep the ice thin. McPhee et al. (2005) suggest that confined zones of upwelling of the pycnocline associated with significant shear motion of sea ice may greatly enhance local ocean-to-ice heat transfer and thinning of the winter ice cover. Thus, the net effect of deformation may be positive or negative especially in a thinning ice cover: the reduction in ice strength in both the seasonal and multiyear ice zones increases deformation and promotes winter ice production in new openings while the oceanographic response may act to reduce the impact on the ice mass balance. Present-day ice-ocean models do not have adequate representation of these small-scale processes (Coon et al., 2007) to fully examine the significance of their atmospheric, oceanographic, or climatic implications (Kwok & Untersteiner, 2011).

Acknowledgments

We thank Lisa Nguyen for her assistance in the preparation of the ice drift data set. The AMSR-E brightness temperature and ice concentration fields are provided by World Data Center A for Glaciology/National Snow and Ice Data Center, University of Colorado, Boulder, CO. This work was carried out at the Jet Propulsion Laboratory, California Institute of Technology, under contract with the National Aeronautics and Space Administration.

References

Coon, M., Kwok, R., Levy, G., Pruis, M., Schreyer, H., Sulsky, D., 2007. Arctic Ice Dynamics Joint Experiment (AIDJEX) assumptions revisited and found inadequate. J. Geophys. Res. 112, C11S90. doi:10.1029/2005JC003393.

Kwok, R., 2001. Deformation of the Arctic Ocean sea ice cover: November 1996 through April 1997. In: Dempsey, J., Shen, H.H. (Eds.), Scaling Laws in Ice Mechanics and Dynamics. Kluwer Academic, pp. 315–323.

Kwok, R., 2004. Annual cycles of multiyear sea ice coverage of the Arctic Ocean: 1999–2003. J. Geophys. Res. 109, C11004. doi:10.1029/2003JC002238.

Kwok, R., 2006. Contrasts in Arctic Ocean sea ice deformation and production in the seasonal and perennial ice zones. J. Geophys. Res. 111, C11S22. doi:10.1029/2005JC003246.

Kwok, R., 2008. Summer sea ice motion from the 18 GHz channel of AMSR-E and the exchange of sea ice between the Pacific and Atlantic Sectors. Geophys. Res. Lett. 35, L03504. doi:10.1029/2007GL032692.

Kwok, R., Cunningham, G.F., 2000. RADARSAT Geophysical Processor System: Data User's Handbook. Jet Propulsion Laboratory JPL D-29149. URL http://rkwok.jpl.nasa.gov/documents/users-master_v1.0.pdf.

Kwok, R., Cunningham, G.F., 2002. Seasonal ice area and volume production of the Arctic Ocean: November 1996 through April 1997. J. Geophys. Res. 107 (C10), 8038. doi:10.1029/2000JC000469.

Kwok, R., Cunningham, G.F., 2010. Contribution of melt in the Beaufort Sea to the decline in Arctic multiyear sea ice coverage: 1993–2009. Geophys. Res. Lett. 37, L20501. doi:10.1029/2010GL044678.

Kwok, R., Untersteiner, N., 2011. The thinning of Arctic sea ice. Phys. Today 64 (4), 36–41.

Kwok, R., Schweiger, A., Rothrock, D.A., Pang, S., Kottmeier, C., 1998. Sea ice motion from satellite passive microwave data assessed with ERS SAR and buoy data. J. Geophys. Res. 103 (C4), 8191–8214.

Kwok, R., Curlander, J.C., McConnell, R., Pang, S., 1990. An Ice Motion Tracking System at the Alaska SAR Facility. IEEE J. Oceanic Engineering 15 (1), 44–54.

Kwok, R., Cunningham, G.F., Wensnahan, M., Rigor, I., Zwally, H.J., Yi, D., 2009. Thinning and volume loss of Arctic sea ice: 2003–2008. J. Geophys. Res. doi:10.1029/2009JC005312

Kwok, R., Toudal Pedersen, L., Gudmandsen, P., Pang, S.S., 2010. Large sea ice outflow into the Nares Strait in 2007. Geophys. Res. Lett. 37, L03502. doi:10.1029/2009GL041872.

Lindsay, R.W., Stern, H., 2003. The RadarSat geophysical processor system: quality of sea ice trajectory and deformation estimates. J. Atmos. Ocean Tech. 20, 1333–1347.

McPhee, M., Kwok, R., Robbins, R., Coon, M., 2005. Upwelling of Arctic pycnocline associated with shear motion of sea ice. Geophys. Res. Lett. 32, L10616. doi:10.1029/2004GL021819.

Stroeve, J., Holland, M.M., Meier, W., Scambos, T., Serreze, M., 2007. Arctic sea ice decline: faster than forecast. Geophys. Res. Lett. 34, L09501. doi:10.1029/2007GL029703.